

Simulation of Shot Peening of Case Hardened Gear Steel

E. Nordin^{1,2}, M. Olsson^{2,*}

1 Scania CV AB, Sweden

2 KTH Material and Structural Mechanics, 100 44 Stockholm,
Sweden

* Contact author: mart@kth.se

Abstract

A material model for predicting fatigue related changes due to shot peening is developed. The model includes plastic behaviour at large strains and transformation of retained austenite. The model is simplified to limit the amount of material parameters needed and an iterative approach is used to fit the parameters to experimental data in the form of uniaxial tests on through hardened specimens, single impacts of carbide balls on polished case hardened test plates and on shot peened, ground test plates. With good accuracy, reasonable computer resources and basic experimental techniques to fit the model parameters, the model can predict; residual stresses, retained austenite transformation and work hardening in form of Vickers hardness increase. The model is also adequate for parameter studies as exemplified by changing media hardness, coverage or media shape variations. For surface roughness predictions, the initial surface roughness of the target must be included and future work is needed there.

1 Introduction

1.1 Shot peening

Shot peening of gears is commonly used to increase the tooth root strength and can benefit surface fatigue depending on the final surface roughness [1, 2]. The main fatigue strength increase is usually attributed to the compressive residual stress induced close to the surface. The normal depth of the compressive residual stress is a few tenths of a millimetre. Other fatigue influencing factors are the work hardening and, in the case of gear steel, the transformation of retained austenite that increases the surface hardness. The surface roughness can also influence the fatigue properties, improving or degrading, depending on the loading and original surface state [3]. The grain size can also decrease due to shot peening which is also beneficial to fatigue. That is commonly referred to as severe shot peening [4]. Something to be careful about is however to avoid over-peening due to too high intensity or excessive coverage which can cause wear and micro cracks to form [5].

The determination of the shot peening parameters to use is an expensive task that would involve several variations of parameters and fatigue testing of each variant. Most shot peening specifications therefore rely on experience and it can thus be assumed that most shot peening is coarsely optimized between the cost and the fatigue improvement. There is therefore a natural desire to simulate shot peening and the improvement in fatigue properties and in that way decrease the number of physical tests.

1.2 Material models

In the case of gear steels it is usually a two phase material consisting mainly of martensite and around 20% retained austenite. From experiments in Nordin and Alfredsson [6] it can be seen that the retained austenite transforms to martensite due to the shot peening. A material model for shot peening of gear steels should therefore include martensite transformation. Although there are many scientific investigations for martensite transformation in austenitic steels there is much less work done for gear steels and especially during shot peening. Most papers dealing with phase transformations concern stainless steels. Sidhoum *et al.* [7] shows a typical application where an austenitic stainless steel, AISI 304L, is tested in bending and an FEM model, implemented in the user material model VUMAT (Abaqus Explicit), is used to compare experimental data to simulated. The model is based on the work by Olson and Cohen [8] in which it is assumed that shear band intersections in the austenite phase are the dominant nucleation sites for strain induced transformation. Stringfellow *et al.* [9] introduce a probability parameter for martensitic transformation to start at a nucleation site. The probability is taken to be a function of temperature and stress state. The stress state is a modifier of the shear bands probability to nucleate martensitic transformation but cannot promote transformation without shear bands. It is also assumed that the deviatoric part of the transformation is directed along the applied stress deviator. Tomita and Iwamoto [10] introduce a strain rate dependence so that the number of shear band intersections increase as the strain rate increases. Later simplifications of the implementation by Serri *et al.* [11] and Sierra and Nemes [12] remove the strain rate dependence. Sierra and Nemes [12] also removes the probability parameter.

Guiheux *et al.* [13] investigate the martensitic transformation in austenitic stainless steel 301LN by single indentation experiments. An air gun was used to shoot a steel ball at the target with 35 and 70 m/s velocities. The material model was implemented in Abaqus Explicit and the model parameters were identified from quasi-static tension tests. Residual stress in radial and tangential direction outside the indent was compared with simulations. The dimensions of the indent were not compared between experiments and simulations except for the pile-up which was overestimated with a factor of three. The material model did not include strain rate effects.

Compared to austenitic stainless steel, the literature is scarce regarding experiments and models for martensitic transformation in gear or bearing steel, where the retained austenite content is around 20% and embedded in a matrix of martensite or bainite structure. Neu and Sehitoglu [14] investigated carburized 4320 steel and observed larger retained austenite transformation in tension than in shear and minor transformation in compression. The amount of transformation for a given axial strain increased with decreasing temperature. Transformation without applied load initiated at -45 °C.

Hazar *et al.* [15] included retained austenite transformation for a martensitic bearing steel previously investigated by Linares Arregui and Alfredsson [16]. The model included both stress and strain induced transformation as well as non-linear isotropic and kinematic hardening. The model did not include strain rate dependent yield stress which would be necessary for shot peening applications where very high strain rates exist.

1.3 Shot peening simulations

Simulation of shot peening has several challenging aspects. There are contact between the ball and target, large deformations and plasticity that must all be handled by the FEM-solver. The impact time is in the order of microseconds and high strain rates occur in the material. Due to the plasticity, the target is also heated which might be important to consider.

Zimmermann and Klemenz [17] presents a comprehensive overview of the finite element models that had been presented up to year 2010. The earliest models up to around year 2000 were limited to 2D simulations due to computer capacity. After that, 3D models became feasible but often with different types of symmetry boundary conditions to decrease the model size. Rigid shots were also often used. Meguid *et al.* [18] use a one-quarter model and a symmetry cell model in a follow up paper where also deformable shots are considered [19]. Schwarzer *et al.* [20] use a full model with infinite elements at the outer edges to remove shock waves in the material from each impact. Rigid shots are used in a symmetric impact pattern. Miao *et al.* [21] introduce a model with randomly distributed impacts at both normal and angled impacts. Comparison for different cases is made for the residual stresses, plastic strain and surface roughness. Surface roughness is also specifically investigated by Bagherifard *et al.* [22] modelling an aluminium target impacted by elastic shots. Comparison with experiments shows a correlation with Ra around 12%. Studying the behaviour for increasing coverage also shows that Ra is the first surface parameter to reach a steady state. This is explained by the fact that Ra is a mean value of the measured area while *e.g.* Rz is the maximum difference between the highest peak and lowest valley.

However, due to the high computational cost, approximations using symmetrical cell models and rigid shots are still presented [23]. When

a large number of simulations need to be run, for example, for optimization of parameters this might still be the only practical option.

This paper introduces a material model for the prediction of the important changes to the material during shot peening from a fatigue point of view, *i.e.* residual stresses, retained austenite content, work hardening and surface topography. The model is also developed with the purpose to be practically useful in shot peening simulations with many indentations, *i.e.* performance and stability at large deformation. Experimental test results and a method to determine the model parameters are presented. A parameter variation of the shot peening model will also be presented to show the influence of a few key parameters.

2 Experiments

2.1 Uniaxial test specimens

Material characterization

The material is case hardening gear steel of the Swedish standard SS 92506, see Table 1 for the material specification. Shaft blanks are manufactured to 2 mm thin plates with a diameter of approximately 70 mm. A small hole is drilled close to the edge by which the plates are hung during the heat treatment. The goal of the heat treatment is to create a through hardened structure that is similar to the near surface case material of gears. The plates are carburized in a pusher furnace for a total of 1420 minutes. The temperature is 935 °C with a carbon potential of 0.8%. The plates are then quenched in 110 °C Quenchway 125B oil. Tempering is done for 2 hours in a temperature of 185 °C.

Table 1: Chemical composition of SS 92506.

C %	Si %	Mn %	P %	S %	Cr %	Ni %	Mo %	Cu %	Al %	N %
0.17- 0.23	max 0.40	0.65- 0.95	max 0.025	0.020- 0.040	0.35- 0.70	0.40- 0.70	0.15- 0.25	max 0.35	max 0.050	0.005- 0.015

To verify that through hardening is achieved one plate is cut and prepared for hardness measurement. Vickers hardness is measured with a Matsuzawa MXT 30 hardness tester with a digital camera and the Buehler Omnimet MHT analysing software. Vickers hardness with a force of 1 kgf is used and with 0.1 mm between the indents. Each indent is offset in height also to avoid interference between measurements. Three series at different positions are performed and the results are shown in Figure 1. There is no tendency for a hardness decrease in the middle of the thickness so the through hardening is successful.

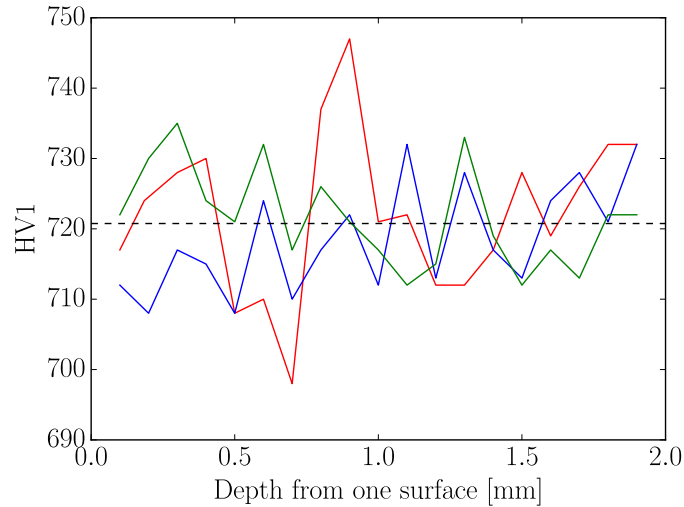


Figure 1: Vickers hardness as function of depth for three series. Mean hardness is 721 HV1 with a standard deviation of 8.9 HV1.

Retained austenite is measured with an Xstress 3000 G3 X-ray diffractometer using Cr-K α radiation. The ferrite phase is measured on planes $\{211\}$ (156.4°) and $\{200\}$ (106.1°) for 20 seconds. The

austenite phase is measured on planes $\{220\}$ (130°) and $\{200\}$ (80°) for 40 seconds. The peak for the ferrite phase is fitted with Split Pearson VII and the background with a linear fit. The peak for the austenite phase is fitted with a Gaussian function and the background with a parabolic function. Four different depths are measured and electropolishing with a Struers Movipol-5 is used to remove the surface material. The results are shown in Table 2 and agree with the retained austenite measurements in [6].

Table 2: Retained austenite content on a through hardened plate.

Depth [mm]	Austenite %	Deviation $\pm\%$
0	14.3	1.3
0.01	14.1	0.8
0.04	22.2	1.9
0.15	21.9	2.4

Stress-strain experiments

Test specimens for tension and compression are cut from the through hardened plates with wire electric discharge machining (EDM). Figure 2 shows the dimension used. The tension specimens have a test length that is long enough to use extensometers to measure the strain in the axial direction. The strain in the transverse direction is measured with two strain gauges, one on each side of the specimen and the average strain of these two are recorded. The specimen is loaded in a servohydraulic testing machine and extended with 0.003 mm/s at a temperature of 25 °C.

For the compression specimens a compromise has to be made between buckling stability, minimum width for strain gauges and the homogeneity of strains over the strain gauge area. A ratio between test length and width of two is determined by FEM-calculations to give acceptable accuracy. Because of the small test length to improve buckling stability the axial strain can not be measured with extensometers. Instead two strain gauges are connected to the 2 mm

thick sides. The transverse strains are measured in the same way but connected to the 3.5 mm sides. The specimen is compressed in a servohydraulic testing machine with 0.001 mm/s at 25 °C.

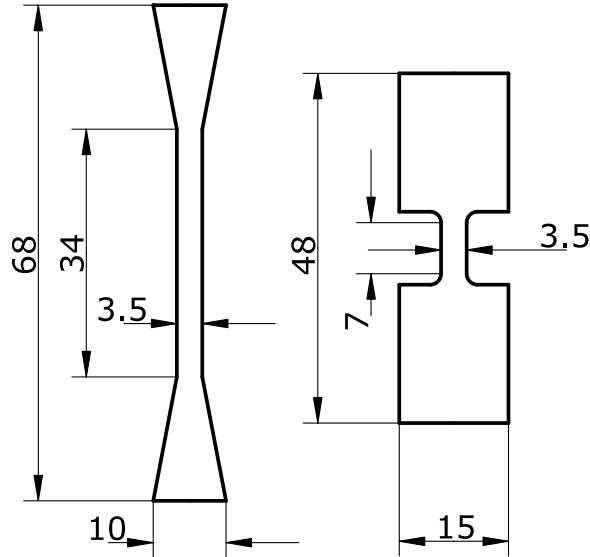


Figure 2: Dimensions in millimetres for tension (left) and compression (right) specimens.

2.2 Single indentation experiment

Dynamic indentations are made with tungsten carbide balls with 1 mm diameter. The balls are shot with an air pressure powered gun, [24]. The ball impact and return velocities were measured with two light sensor gates. The gates are positioned 68.5 ± 0.2 mm apart and the time difference between the two gate signals is measured both with an Arduino and with an oscilloscope with an estimated accuracy of 4 μ s. Five different velocities are used and 10 separate impacts are made at each velocity. The indentations are made on mirror polished, case hardened, plates with dimensions 30x30x10 mm, [6]. Each indent is measured in a PL μ 2300 confocal microscope from Sensofar. The width of each measurement is 5 times the radius of the indent to

include plate surface that is un-affected by the pile-up. Levelling and offsetting the outer boundary to zero is done using the analysis software SensoMap 4.1. An example of the resulting 3D image of an indent is shown in Figure 3a. A 2D profile is extracted through the centre of the indent. Definitions of depth and pile-up are shown in Figure 3b. The radius of the indent is chosen as the position where a fitted spherical shape would start deviating from the profile. Because the exact position is not critical this is judged optically.

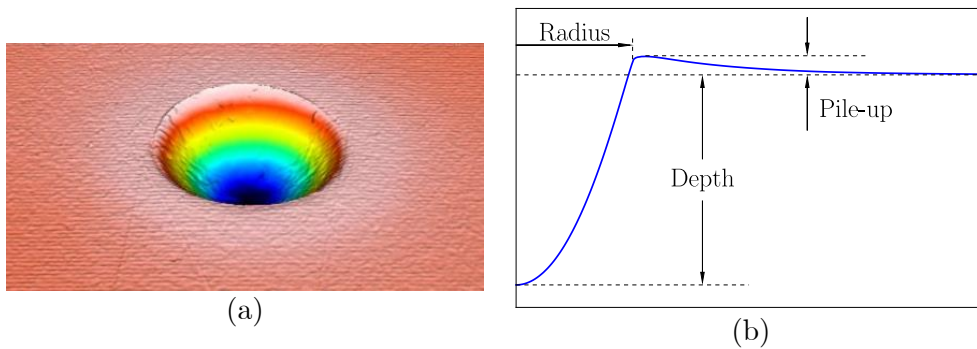


Figure 3: Indentation measured with confocal microscope in (a). Profile extracted through centre of indent with definition of depth and pile-up in (b). The estimated position of the indent radius is also indicated.

2.3 Shot peening experiments

The shot peening experiments are explained in detail in [6] and only a short summary is presented here. Test specimens with dimensions 30x30x10 mm are cut from gear blanks of SS 92506 steel. The surface is ground to a surface roughness similar to normal gear flanks (around $R_a = 0.5 \mu\text{m}$). The plates are case-carburized and quenched in a pusher furnace used for gear heat treatment. After tempering the surface hardness measure 716 HV1 and a case depth of 1.7 mm. The plates are then representative of gear flanks.

The shot peening is performed in a compressed air shot peening machine. The steel plates are assembled on a round, rotating, table so that each plate pass beneath two shot peening nozzles. An Almen holder is used to set the shot peening parameters to get Almen intensities of 0.22 mm A, 0.34 mm A and 0.49 mm A for 0.7 mm media. A smaller diameter media of 0.35 mm, which is normally used for a second stage double shot peening, is also used with an Almen intensity of 0.24 mm A. Coverages of roughly 100%, 200% and 400% were used. The plates are later measured in different ways and results that will be used in this paper include residual stresses, residual austenite, Vickers hardness and surface roughness.

3 Material model formulation

Constitutive models are frequently based on the work of Tomita and Iwamoto [10]. Sierra [12] simplified the implementation by removing the probability distribution function for a shear band intersection. Since this work deals with steels that are in majority of martensitic phase and only about 20%, or less, austenitic a further simplification is introduced by removing the separate flow functions for the martensite and austenite phase. A single flow stress function is used and the increase in flow stress, due to transformation, is handled by an increase in yield stress. Also, during the parameter fitting it was noticed that there was little improvement to include shear band induced transformation. To simplify the parameter fitting and decrease the number of unknown parameters, shear based transformation was excluded and only stress-based transformation is used.

The constitutive behaviour is chosen as a Johnson-Cook formulation where the flow stress σ_y is written as

$$\sigma_y = \sigma_{qs} \cdot f_{RD} \cdot f_T , \quad (1)$$

where σ_{qs} is the quasi-static flow stress at reference temperature, f_{RD} is the rate dependent factor (≥ 1) and f_T is the temperature dependent factor. The rate dependence f_{RD} is

$$f_{RD} = 1 + C \ln\left(\frac{\dot{\epsilon}^{pl}}{\dot{\epsilon}_0}\right), \quad (2)$$

where $\dot{\epsilon}^{pl}$ is the equivalent plastic strain rate and C is a material parameter with the reference strain rate chosen to $\dot{\epsilon}_0 = 1 \text{ s}^{-1}$. If $\dot{\epsilon}^{pl}$ is lower than $\dot{\epsilon}_0$, f_{RD} is set to 1. The temperature dependence is written as

$$f_T = 1 - \left[\frac{(T - T_{ini})}{(T_{melt} - T_{ini})} \right]^{m_T}, \quad (3)$$

when the temperature T is between the reference temperature T_{ini} and the melting temperature T_{melt} . If T is below T_{ini} the factor is set to 1. The exponent m_T is a material parameter.

The von Mises yield criterion is used which gives the yield function

$$F = \sigma_e^b - \sigma_y = \sqrt{\frac{3}{2} (s_{ij} - x_{ij}^{dev})(s_{ij} - x_{ij}^{dev})} - \sigma_y, \quad (4)$$

where σ_e^b is the equivalent von Mises stress with respect to the back stress, s_{ij} is the deviatoric stress tensor and x_{ij}^{dev} is the deviatoric part of the back stress tensor. Three independent evolving back stress tensors are used which are super positioned according to Chaboche [25]. The evolution of each back stress tensor is given by the kinematic hardening rule according to Armstrong and Frederick [26].

$$\dot{x}_{ij}^{(k)} = C_k \frac{\sigma_{ij} - x_{ij}}{\sigma_y} \dot{\epsilon}^{pl} - \gamma_k x_{ij} \dot{\epsilon}^{pl}, \quad (5)$$

where C_k and γ_k are material parameters and the total back stress tensor is

$$x_{ij} = \sum_k x_{ij}^{(k)}. \quad (6)$$

The quasi-static yield stress σ_{qs} is divided in two parts

$$\sigma_{\text{qs}} = \sigma_{\text{fs}} + \sigma_{\text{inc}}, \quad (7)$$

where σ_{fs} is the slip based plasticity evolving flow stress following equations 4 - 6 and σ_{inc} is the increase in yield stress due to austenite transforming to martensite. The yield stress increase is computed with

$$\sigma_{\text{inc}} = \left(\frac{\Delta\sigma_m}{1-f_{m,\text{ini}}} \right) f_m^{\text{inc}}, \quad (8)$$

where $\Delta\sigma_m$ is a material parameter for the yield stress increase for transformation from the starting content $f_{m,\text{ini}}$ to 100% martensite and f_m^{inc} is the increase in martensite content during the simulation.

The plastic strain rate is split in a slip deformation component and a transformation component, the later also split into a deviatoric (shape) change and a dilatational (volume) change as

$$\dot{\varepsilon}_{ij}^{\text{p}} = \dot{\varepsilon}_{ij}^{\text{pslip}} + \dot{\varepsilon}_{ij}^{\text{pshape}} + \dot{\varepsilon}_{ij}^{\text{pdilat}}. \quad (9)$$

The evolution of the slip strain is assumed to be normal to the yield surface as

$$\dot{\varepsilon}_{ij}^{\text{pslip}} = \frac{3}{2} \frac{s_{ij} - x_{ij}^{\text{dev}}}{\sigma_y} \dot{\varepsilon}^{\text{pl}}. \quad (10)$$

The shape change is assumed to be in the direction of the deviatoric stress [9, 10]

$$\dot{\varepsilon}_{ij}^{\text{pshape}} = R_s \frac{s_{ij}}{\sqrt{2/3}\sigma_e} \dot{f}_m, \quad (11)$$

where σ_e is the von Mises equivalent stress, \dot{f}_m is the change in martensite content and R_s is a parameter that controls the magnitude of the shape change. The dilatational strain rate due to the phase transformation is

$$\varepsilon_{ij}^{\text{pdilat}} = \frac{1}{3} \Delta V \dot{f}_m \delta_{ij} , \quad (12)$$

where ΔV is a material parameter for the volume change when austenite transforms to martensite.

3.1 Transformation model

The martensite fraction f_m is assumed to follow the Koistinen-Marburger equation [27]. To include influence from the stress state ΔM_σ and tempering M_T , these additional terms are added which gives

$$f_m = 1 - e^{-k(M_s + \Delta M_\sigma + M_T - T)} , \quad (13)$$

where M_s is the martensite start temperature and T the current temperature. The factor k is computed as

$$k = \frac{4.605}{M_s - M_f} , \quad (14)$$

where M_f is the martensite finish temperature, defined as the temperature when 99% of the austenite has transformed to martensite.

It is well known that a hydrostatic tensile stress will promote retained austenite transformation while hydrostatic compressive stress will reduce it, Stringfellow *et al.* [9]. A shear stress will also promote transformation and therefore Denis *et al.* [28] formulated an equation with hydrostatic stress and the von Mises equivalent stress; $\Delta M_\sigma = a_1 \sigma_m + a_2 \sigma_e$. During the parameter fitting in this work, this was judged to not be fully adequate to fit the experimental data, so an additional term using the third deviatoric stress invariant J_3 was added, as in Kubler *et al.* [29]. With the addition of the $a_3 J_3$ term, it was noticed that the hydrostatic term did not have a significant contribution. This means that in the material model, the hydrostatic stress term can be omitted when the term with the third deviatoric

stress invariant is used. The shift in martensitic start temperature due to applied stress is therefore written as

$$\Delta M_\sigma = a_2 \sigma_e + a_3 J_3 , \quad (15)$$

where σ_e is the von Mises equivalent stress, J_3 is the third deviatoric stress invariant and a_2 , a_3 are material parameters.

Tempering the steel after quenching will stabilize the retained austenite and there will therefore be a limiting value of stress or temperature before the transformation can continue. This is included as a shift in temperature, M_T . To fulfil initial conditions for equation (13) the martensite shift is computed as

$$M_T = -\frac{1}{k} \ln(1 - f_{m,ini}) - M_s - a_2 \cdot \sigma_{lim} + \frac{2a_3}{27} \cdot \sigma_{lim}^3 + T_{ini} , \quad (16)$$

where $f_{m,ini}$ is the fraction of martensite initially, σ_{lim} is the uniaxial tension stress that initiates stress-assisted transformation and T_{ini} is the initial temperature.

The above described model is implemented in Abaqus user subroutines UMAT/VUMAT using a general scheme of elastic predictor and plastic corrector algorithm. Transformations are computed and the martensite content increased. The yield stress is then updated before yielding is checked. If the material is yielding, the kinematic back stresses are updated. In an explicit analysis, where the time step is very small, the equivalent plastic strain will influence the martensitic transformation in the next time step. For an implicit analysis, the martensitic transformation and yielding will be converged using a Newton-Raphson scheme. The state variables are updated and the dissipated inelastic specific energy (PENER) is computed which Abaqus use to increase the temperature of each element. An inelastic heat fraction equal to 0.9 is used which means that 90% of the plastic work will be converted to heat.

3.2 Vickers hardness calculation

The Vickers hardness value is computed from the flow stress of the simulation at each element using the method by Mata and Alcalá [30],

$$\frac{H}{\sigma_r} = -0.0023 \left[\ln \left(\frac{E}{\sigma_r} \right) \right]^4 + 0.0647 \left[\ln \left(\frac{E}{\sigma_r} \right) \right]^3 - 0.6817 \left[\ln \left(\frac{E}{\sigma_r} \right) \right]^2 + 3.1968 \left[\ln \left(\frac{E}{\sigma_r} \right) \right] - 2.9261 . \quad (17)$$

The flow stress σ_r in equation (17) is computed in the VUMAT code as

$$\sigma_r = \sigma_{fs} + \left(\frac{\Delta\sigma_m}{1-f_{m,ini}} \right) f_m^{inc} + \sum_{k=1}^3 \frac{C_k}{\gamma_k} \left(1 - e^{-\gamma_k \cdot (\bar{\epsilon}^{pl} + 0.08)} \right) , \quad (18)$$

which is the initial flow stress, increase due to martensitic transformation and the kinematic hardening from 0.08 plastic strain increase (Vickers hardness strain), respectively.

4 Simulation

The model parameters can be iteratively fitted using the tension and compression experiments together with the impact results for indent radius, depth and pile-up. Some parameters are determined solely from the literature or computational programs while for others reasonable starting values for the iteration are chosen.

Using a carbon content of 0.8 wt% carbon in the case, the volume expansion from retained austenite to martensite is calculated according to [31]. The martensite start, M_s , and finish, M_f , temperatures are computed using the material properties simulation software JMatPro [32], using the chemical composition in Table 1 and 0.8 wt% carbon. Starting value for the shape change parameter is chosen according to [10].

The elastic modulus E and the Poisson's ratio ν is determined from the initial slopes of the stress - axial strain and transverse strain - axial strain tests. Interestingly there is a slight difference between the tension and compression experiments. In tension the results are $E = 195$ GPa and $\nu = 0.27$ while the compression results are $E = 205$ GPa and $\nu = 0.3$. However, it is not deemed necessary to include a stress differential effect for the elastic part so the values $E = 200$ GPa and $\nu = 0.27$ are chosen.

Initial yield limit σ_0 and the kinematic hardening factors is chosen to fit the uniaxial compression experiments.

The factor for the start of stress induced transformation, σ_{lim} , is determined from the uniaxial tension experiments as the stress when the stress-strain curve changes slope from the initial elastic part. The slope of the stress-strain curve after stress induced transformation has started is dependent on the rate of transformation which depends on the a_2 and a_3 factors but also on the shape change factor R_s . The shape change factor must be chosen based on the amount of transformation due to the von Mises stress below the impacting ball at depths below the slip based plasticity. It must therefore be fitted from the impact experiments. The shape factor determines the relation between transverse and axial strains.

4.1 Single indentation simulation

Since the indentation model only involves one ball impacting the target an axisymmetric model can be used as shown in Figure 4. The target is modelled using a quarter circle with a radius of 20 times the impacting ball radius. The outer edge of the circle is meshed with infinite elements that attenuate the shock waves from the impact and decrease vibrations. The centre part of the target, where the ball impact, is meshed with 100 elements on the estimated indentation radius. The surrounding outer part of the target is meshed with

progressively larger elements. Boundary conditions according to Figure 4 are applied. At the start of the simulation, the ball is given a downward velocity. The impact time is estimated as [33]

$$\tau = 2.87 \left(\frac{m_b^2}{R_b E^{*2} v} \right)^{1/5}, \quad (19)$$

where m_b is the mass, R_b the radius and v the velocity of the ball. Here, E^* is the equivalent elastic modulus between the ball and target. The total simulation time is set to 4 times the impact time which removes all vibrations on the target surface. The element type is CAX4RT and the Abaqus 2019-5 Explicit solver is used.

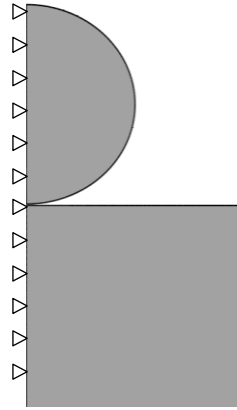


Figure 4: Axisymmetric simulation model. Target has infinite elements at its outer boundary.

4.2 Shot peening simulation

4.2.1 FEM-model

The FEM-model is shown in Figure 5. The target in Figure 5a comprises of an inner square evaluation target, with the same relative size as the Lombardo [34] measurement area used to determine the

impact locations. The side of the square (L) is the, estimated, mean indent diameter divided by the side ratio used in the Lombardo simulation. The mean indent diameter d is estimated before the simulation is set-up by [35]

$$d = 2D\sqrt{v} \left[\frac{\rho}{6P} \right]^{\frac{1}{4}}, \quad (20)$$

where D is the ball diameter, v is the ball velocity, ρ is the ball density and P is the mean dynamic yield pressure. The value of P is fitted to one ball simulations at different velocities. For the material properties of the target and ball used here the value is $P = 5.79$ GPa.

Outside the evaluation area, a cylindrical section is added, having a radius of $0.5L+d$. This section has the same material properties as the evaluation area. Outside that, an elastic section is added with a radius of $1.5L+d$. The envelope surface of the cylindrical model is covered in infinite elements that dissipate shock waves from the ball impacts. The height of the upper part is chosen so that all plastic effects from the impacts are above that level. By reference calculations a depth of $1.15d$ was decided to be adequate. A bottom part with elastic material formulation is added for inertia and to allow shock waves to expand away from the evaluation area. A layer of infinite elements is also added at the bottom of the cylinder.

The mesh size in the evaluation target area is chosen to 20 elements per indent diameter. The ratio of indent diameter to evaluation target side length is chosen to 0.4. This means that the number of elements per side length of the evaluation area is $20/0.4 = 50$. Total number of C3D8RT elements in evaluation area is 55000 and for the whole target 168000. Each ball has 2860 C3D8RT elements.

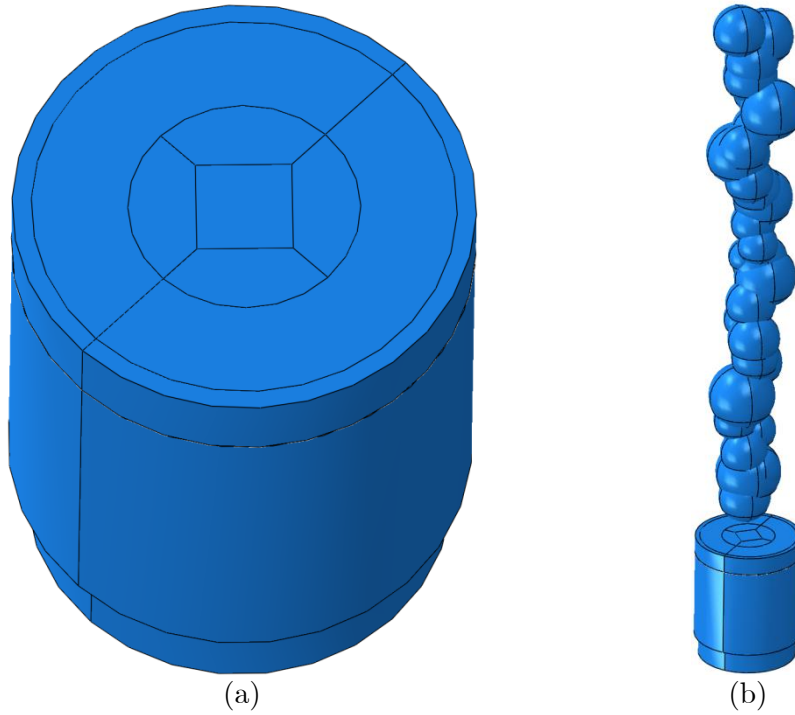


Figure 5: FEM-model of the target in (a), example with 30 spheres positioned above the target in (b).

4.2.2 Media shape

The shape of cut wire media is not perfectly spherical but instead multifaceted. The curvature of the ball at impact position might therefore vary from much smaller to much larger than the nominal radius. The use of ellipsoidal media shape has previously been investigated by [18]. This was also considered in this work but eventually disregarded due to the large number of variations when considering media shapes, coverage ratio and impact patterns. Completely spherical balls gave practically useable results and therefore investigation of details is recommended for future studies.

4.2.3 Media material model

Measured Vickers hardness for the balls are 742 HV1 [6] which is translated to a flow stress at 8% plastic strain of 3092 MPa using [30]. A Johnson-Cook hardening model is used to model a stress-strain curve going through the flow stress point.

$$\sigma_{fs} = [A + B(\bar{\epsilon}^{pl})^n] . \quad (21)$$

The parameters for the ball material are shown in Table 3.

Table 3: Parameters for ball material.

$E = 206 \text{ GPa}$	$A = 1200 \text{ MPa}$
$\nu = 0.3$	$B = 3100 \text{ MPa}$
$\rho = 7850 \text{ kg/m}^3$	$n = 0.2$

4.2.4 Media velocity

The intensity, measured in Almen, is mostly a function of the velocity of the media. In a production environment this is usually not measured so a conversion from Almen intensity to media velocity must be made to simulate the shot peening. Nordin and Alfredsson [24] present a relation of Almen intensity versus velocity for the media and targets used for the experimental results in [6], which will be used to compare the simulation results of the present paper. The media velocities are shown in Table 4.

Table 4: Intensities and corresponding velocities for the used shot peening media.

Denomination	Intensity [mm A]	Media size [mm]	Velocity [m/s]
iD	0.24	0.36	76
i1	0.22	0.84	24
i2	0.34	0.84	34
i3	0.49	0.84	49

4.2.5 Coverage

Coverage is the ratio of area that has been hit by at least one impact. In production it can either be estimated from visual inspection with a microscope or by wearing off a fluorescent paint layer. Full coverage is defined as when more than 98% of the area has been hit. This is of course very dependent on the observer so the time to full coverage should be understood to have a quite large scatter. In a simulation however, the coverage can be determined for each ball impact. The simulation method by Lombardo [34] is here used to determine an impact sequence for the FEM-simulation. The method randomly places filled circles, representing the indent area on a measurement grid and the coverage can then be computed by recording each grid point that has been inside an indent area. Figure 6 shows the pattern used where the coverage (CR) is 100%, the area strike ratio (ASR), defined as the total area of all indent areas within the measurement grid, is 278%. The number of impacts is 33. The ratio of indent diameter divided by the length of one side of the measurement area is 0.4.

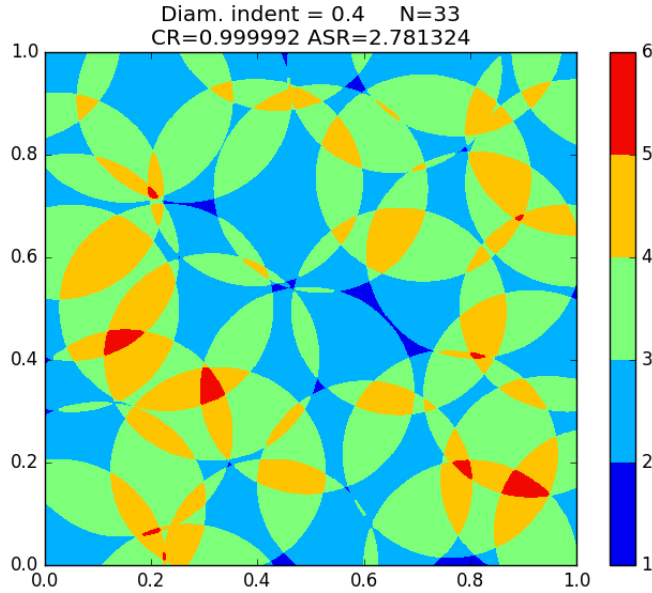


Figure 6: Pseudo random indentations that have covered 100% of the target area with 33 impacts.

The number of impacts in a shot peening simulation decides the total amount of simulation time and it has therefore been many creative ways developed to minimize the impacts [17]. Depending on the material and what resulting parameters that should be evaluated and the accuracy wanted, this can be more or less adequate. In the later years, when the computer capacity has evolved enough, more simulations with random impact patterns have been used [34]. In this paper the Lombardo method is used as a base to decide suitable impact patterns to reach full coverage. Lombardo simulations of random impact patterns are searched for that have a reasonable number of impacts to reach full coverage. Some positions are finally tweaked by hand to avoid repeated impacts close to the same locations.

4.3 Material model parameter determination

Based on the uniaxial tests and the indentation experiments the model parameters in Table 5 are determined. Figure 7 shows the

uniaxial tension and compression curves comparing experimental results with simulated. Stresses are represented well in both tension and compression. The simulation predicts a lower transverse strain than the experimental results for high compressive axial strains.

Table 5: Material model parameters.

$E = 200 \text{ GPa}$	$M_s = 176 \text{ }^\circ\text{C}$	$C_1 = 6 \cdot 10^3 \text{ MPa}$	$\sigma_{\text{lim}} = 490 \text{ MPa}$
$\nu = 0.27$	$M_f = -91 \text{ }^\circ\text{C}$	$\gamma_1 = 4$	$a_2 = 0.05 \text{ }^\circ\text{C}/\text{MPa}$
$\sigma_0 = 1300 \text{ MPa}$	$m_T = 1.0$	$C_2 = 40 \cdot 10^3 \text{ MPa}$	$a_3 = 2 \cdot 10^7 \text{ }^\circ\text{C}/\text{MPa}^3$
$C = 0.008$	$T_{\text{melt}} = 1500 \text{ }^\circ\text{C}$	$\gamma_2 = 80$	$\Delta\sigma_m = 700 \text{ MPa}$
$\dot{\epsilon}_0 = 1.0 \text{ s}^{-1}$	$T_{\text{ini}} = 26 \text{ }^\circ\text{C}$	$C_3 = 300 \cdot 10^3 \text{ MPa}$	$\Delta V = 0.02$
$\rho = 7850 \text{ kg/m}^3$		$\gamma_3 = 400$	$R_s = 0.025$

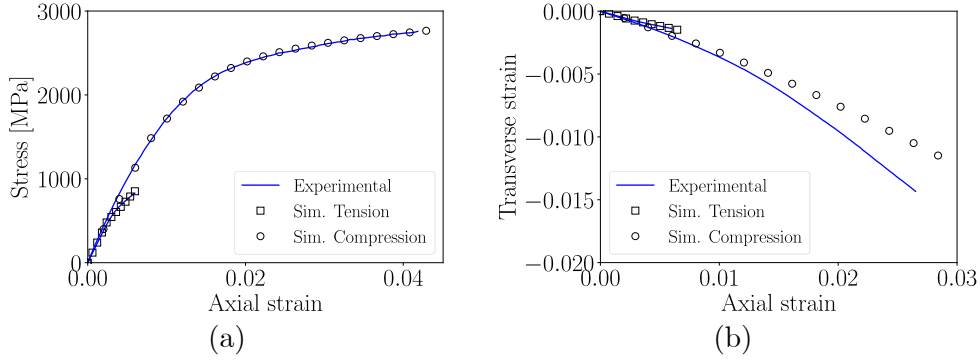


Figure 7: Comparison between experiment and simulation. Stress versus axial strain in (a). In (b) the transverse strain versus axial strain. Compression values have changed sign.

Figure 8 shows the experimentally determined indent radius, depth and pile-up compared to the simulated results. The mean velocities from the experiments are 19.4, 35.9, 51.2, 76.1, 89.5 m/s. The indent radius trend decrease with increasing velocity and the indent pile-up tends to increase more with increasing velocities. It can be seen that it is a clear linear trend between indent depth and velocity although complicated relations between kinematic hardening, temperature effects, strain rate and martensite transformation exist. The relative deviations between experimental mean values and simulated values are less than 2% for indent radius and around 5% for indent depth

and pile-up. Figure 9 shows all the measured indentation profiles together with the simulated result for the five different velocities.

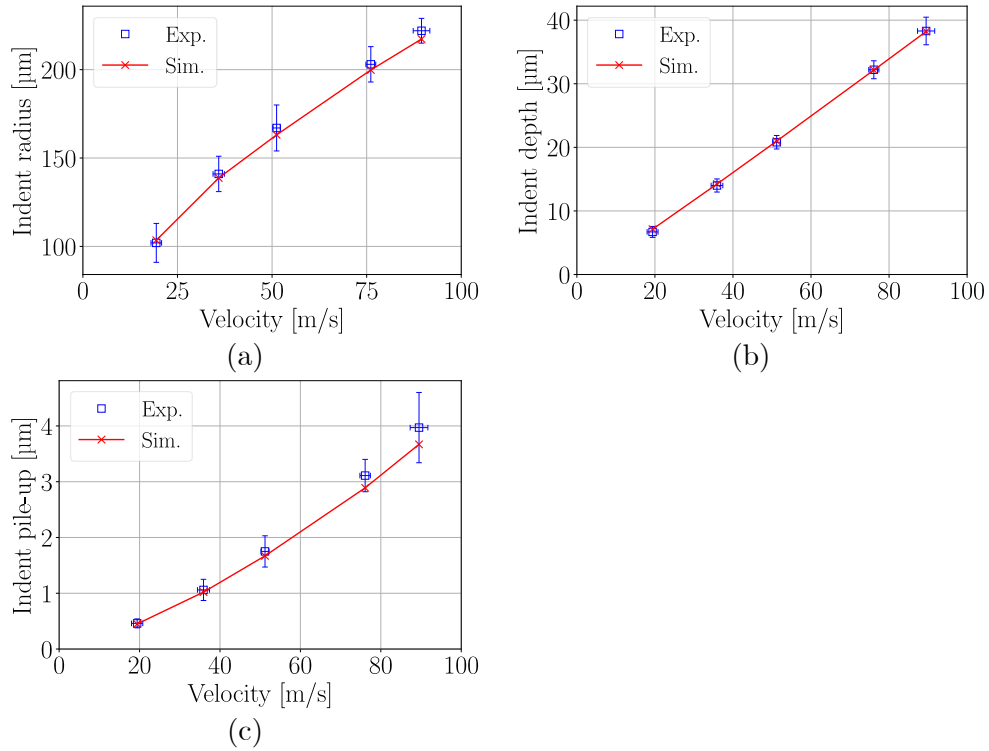


Figure 8: Experimental results compared with simulated results for indentation radius (a), indentation depth (b) and indentation pile-up (c).

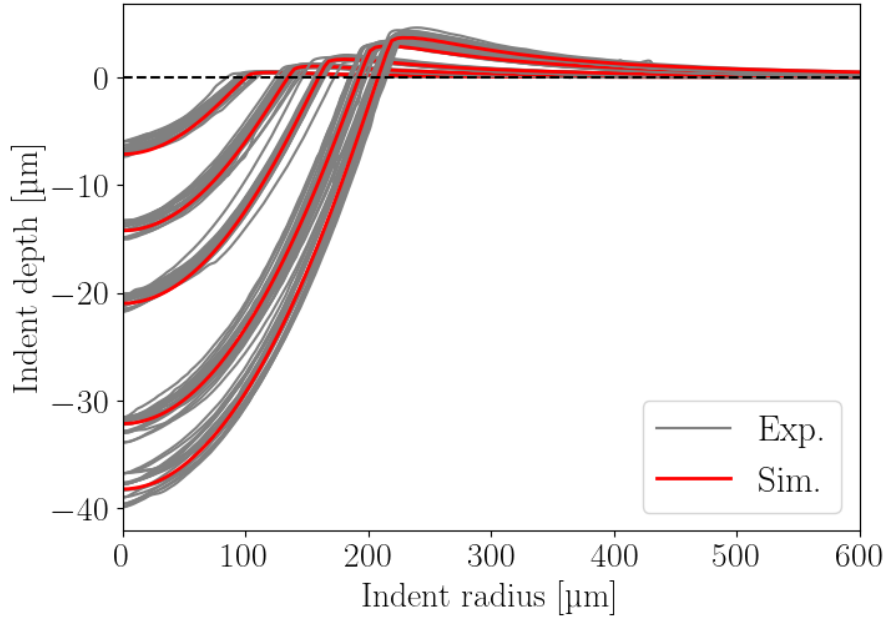


Figure 9: Experimental indentation profiles compared to simulated profile for average velocities 19.4, 35.9, 51.2, 76.1 and 89.5 m/s, respectively.

5 Results

In the following plots, black diamonds, denoted as CH, show the Case Hardened state, before shot peening.

5.1 Residual stresses

Figure 10 shows a comparison of the measured and the simulated residual stresses. The maximal compressive stresses are predicted well as is the overall stress-depth relation. The largest deviation is the stresses closest to the surface where the model predicts close to zero residual stress at the surface while the experimental stresses are around -700 MPa. A probable reason can be that perfectly spherical balls were used here, compare to the results in Subsection 5.9.

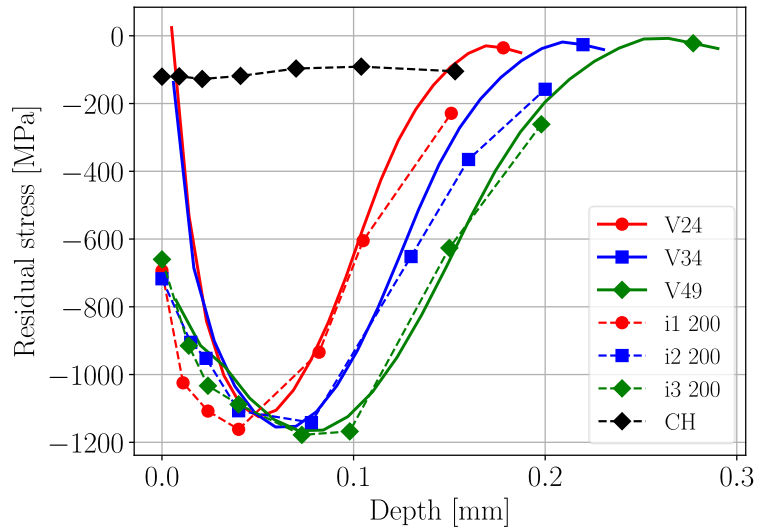


Figure 10: Residual stresses from experiment (dashed lines) and simulation (continuous lines).

5.2 Retained austenite

Figure 11 shows a comparison of the measured and the simulated retained austenite content. Generally the behaviour of the model follows the experimental results although with a larger spread. The experimental results show very little correlation to the impact velocities. Also here this could be caused by the spherical shape with constant size of the balls as the “pointed shape” results in Subsection 5.9 indicate.

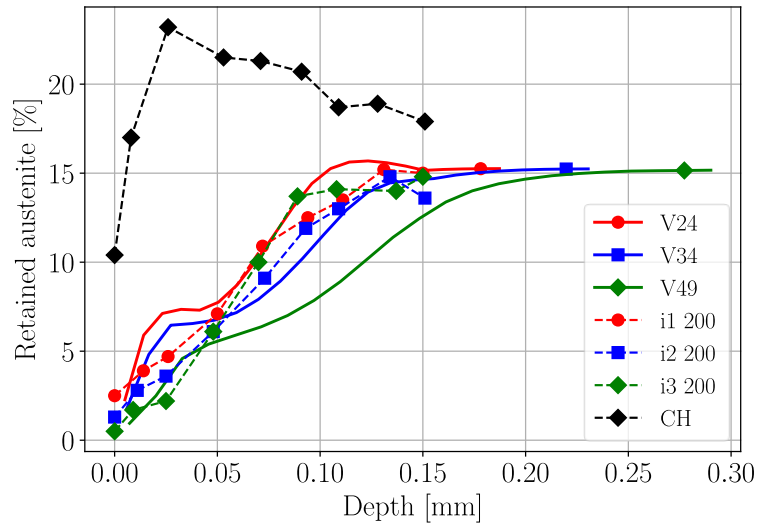


Figure 11: Retained austenite comparison from experiment (dashed lines) and simulation (continuous lines).

5.3 Hardness

Figure 12 shows a comparison of the measured and the simulated Vickers hardness. The simulated results seem to tend to predict hardness changes less deep than the experimental results. No mechanical variation seems to be able to create deeper changes so this might be a deficiency of the material model.

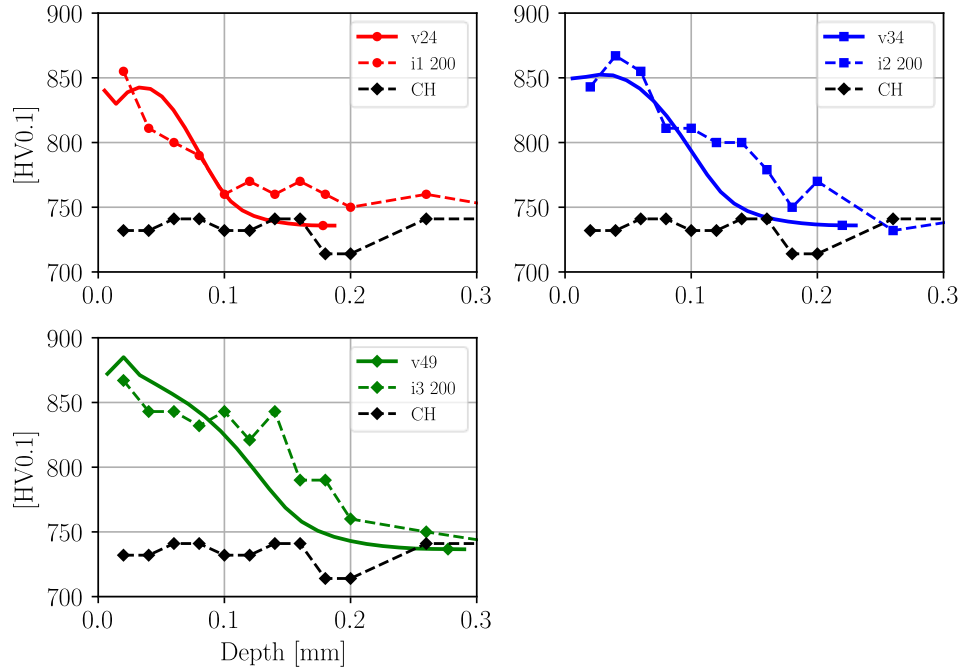


Figure 12: Comparison of Vickers hardness from experiments (dashed lines) and simulation (continuous lines).

5.4 Surface roughness

Surface topography from confocal measurements of the shot peened plates and simulated results are shown in Figure 13. Table 6 shows measured and computed Ra (Sa for simulations). It is clear that the surface roughness values are not similar. The experimental shot peening is not done on polished plates because conditions similar to gears is wanted. The simulations, however, start with a completely flat surface. In general, a rough and polished surface should trend towards the same surface roughness during shot peening but that might not be the case for these conditions. For a true comparison between experimental and simulated surface roughness results, either the experimental plates should be polished before shot peening or the simulated target should have a texture corresponding to the case

hardened plates. None of the options are pursued further and left for future work. Simulating a rough (ground) surface would create considerable added complexity both for the model creation and for numerical FEM challenges. To understand how surface roughness is developed on ground gears, this is however the only option.

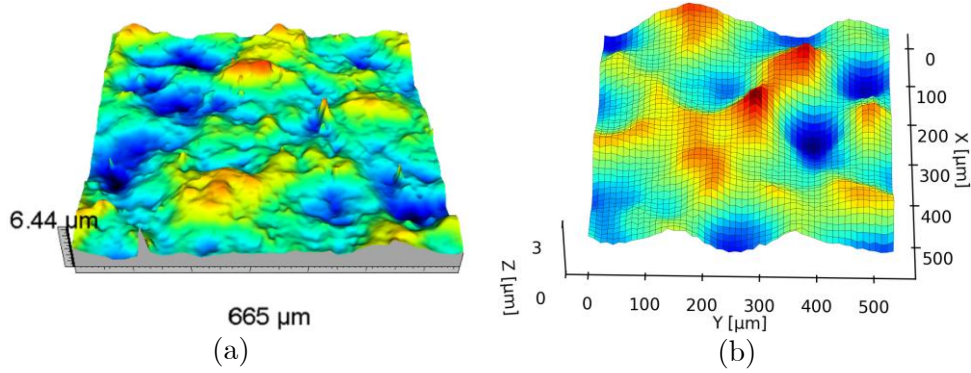


Figure 13: Comparison of surface roughness from experiments (a) and simulation (b).

Table 6: Ra [μm] for experimental and simulated results with 200% coverage.

	Experimental	Sim. Spherical	Sim. Pointed	Sim. Flat
iD	0.83	0.32		
CH	0.50	0	0	0
i1	0.66	0.28	0.48	0.11
i2	0.75	0.39	0.53	0.17
i3	0.78	0.57	0.55	0.29

5.5 Verification with iD media

The material and model parameters were adapted for the i1, i2 and i3 shot peening results. Figure 14 shows residual stresses for three different experimental coverages and simulated results with iD media. The simulated curve seems to fit closest the experimental 400%

coverage results and the experimental 200% coverage curve does not fall in between 100% and 400% curves. This is probably due to limitations in coverage control within the experimental setup. Figure 15 shows the retained austenite. Only three positions in depth were measured for the 100% and 400% coverage plates due to time restraints and capacity problems at the measurement laboratory. Overall the measurements and simulation results agree well and the high retained austenite at the second depth below the surface for the 200% coverage plate is not shown for the 100% and 400% plates. For the Vickers hardness shown in Figure 16, the simulated values are slightly shallower than the experimental results. The peak values close to the surface agree well, however. Overall the model extrapolates well to a smaller media with higher velocity.

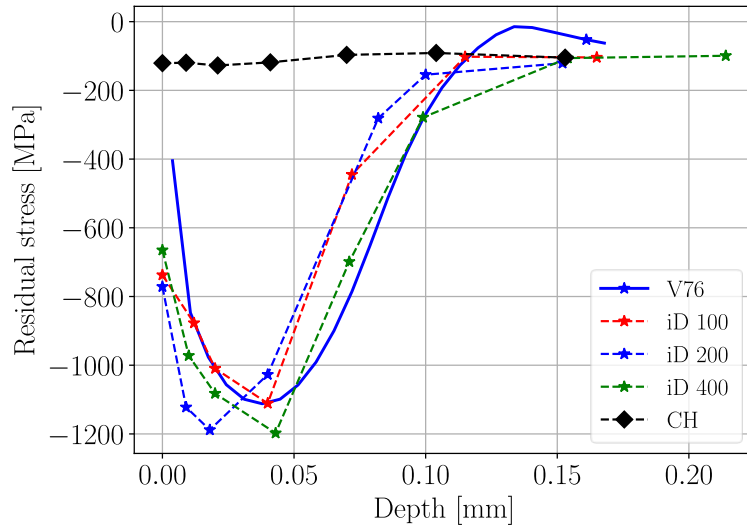


Figure 14: Residual stress for iD media with varying experimental coverage.

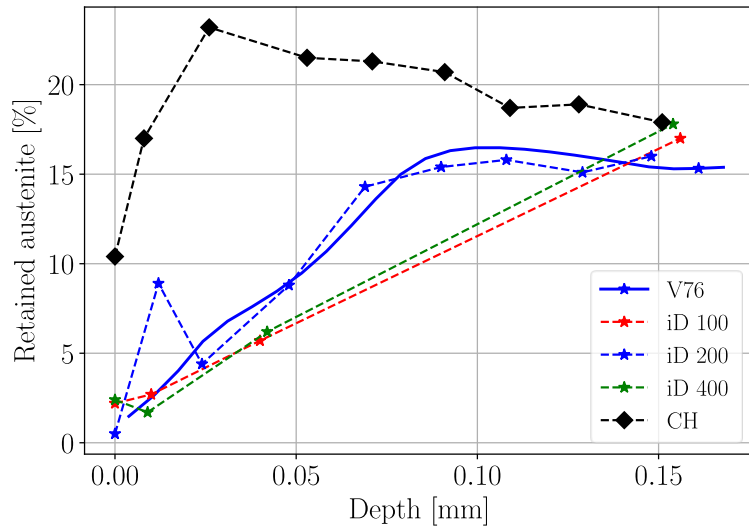


Figure 15: Retained austenite for iD media with varying coverage. Note that only three depths were measured for iD 100 and iD 400 due to time constraints.

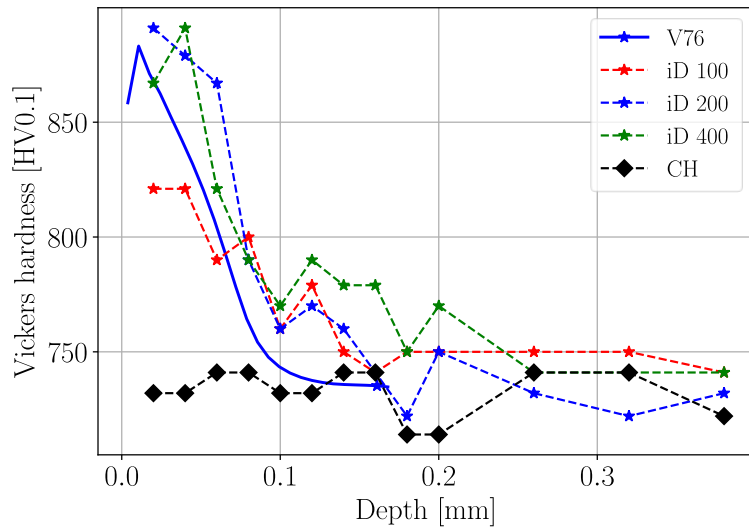


Figure 16: Vickers hardness for iD media with varying coverage.

5.6 Media hardness variation

The nominal media hardness from the experiments is 742 HV with a standard deviation of 50 HV. Simulated results with low hardness of 642 HV, nominal hardness and high hardness of 842 HV are shown in Figure 17, Figure 18 and Figure 19 for residual stresses, retained austenite and Vickers hardness respectively. The residual stresses in Figure 17 show that the only change is the level of the maximum compressive stress obtained. Depths of maximum stress are practically unchanged. Observe here that the velocity of the media is constant in all cases but the Almen intensity, as measured on an Almen plate, would be changed due to the different media hardnesses. Retained austenite in Figure 18 shows transformation at deeper depth for increased media hardness. Tendencies for a local minimum for the retained austenite around the depth of maximum compressive residual stress are seen for the high hardness media.

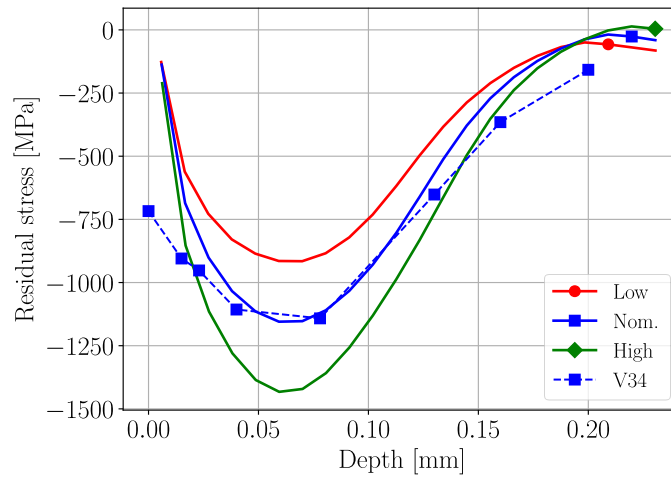


Figure 17: Measured residual stress with impact velocity 34 m/s and simulated media hardness; Low = 642 HV, Nominal = 742 HV, High = 842 HV.

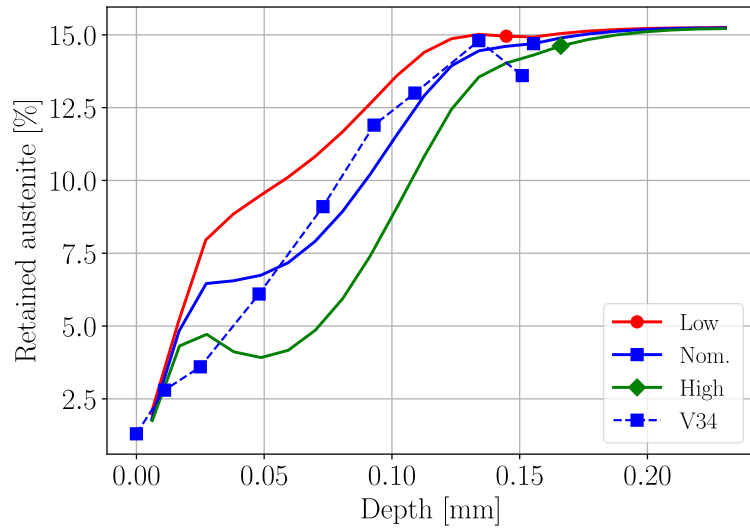


Figure 18: Measured retained austenite with impact velocity 34 m/s and simulated media hardness; Low = 642 HV, Nominal = 742 HV, High = 842 HV.

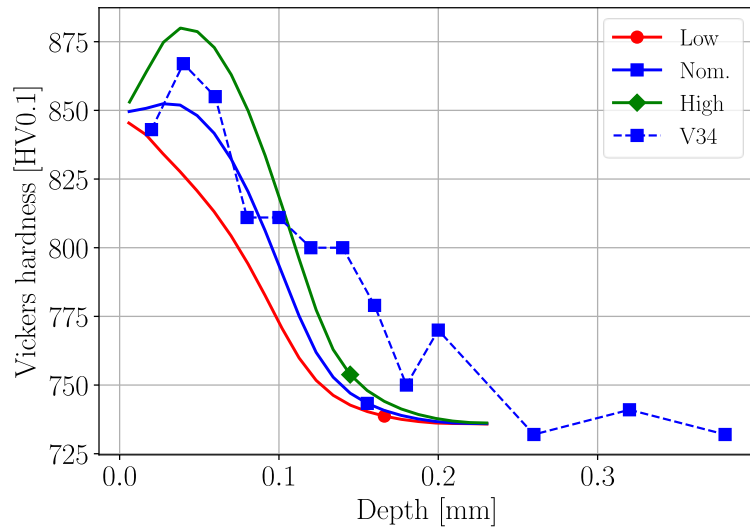


Figure 19: Measured Vickers hardness HV0.1 with impact velocity 34 m/s and simulated media hardness; Low = 642 HV, Nominal = 742 HV, High = 842 HV.

Finally, for the Vickers hardness in Figure 19, all the simulated curves seem to converge around 850 HV at the surface but the harder media creates a maximum in hardness around the depth of maximum residual stress. The three curves suggest that a maximum in hardness below the surface occurs when the media hardness is harder than the target.

5.7 Simulated coverage percent

Determining experimental coverage with, for example, a Peen Scan pen as is done in this work is a quite coarse method and the repeatability of coverage is highly dependent on the machine setup and number of passes that the shot peening stream passes over the target. Extensive simulations can be undertaken in order to understand how much random impact patterns and coverage influence results, using *e.g.* DEM simulations as in [36, 37]. This is left for future work and, instead, a simplified indication of coverage dependence is shown. The impact pattern chosen had 33 balls and in the following plots results for 10th, 20th and 33rd ball impact are shown. Figure 20 shows the change in residual stress for increasing number of impacts. With only 10 impacts the stresses are far from the experimental results. With 20 impacts the stresses are closer but with the impact pattern chosen, around 30 balls are needed in order to reach the experimental stress. A similar trend is seen for both the retained austenite in Figure 21 and the Vickers hardness in Figure 22.

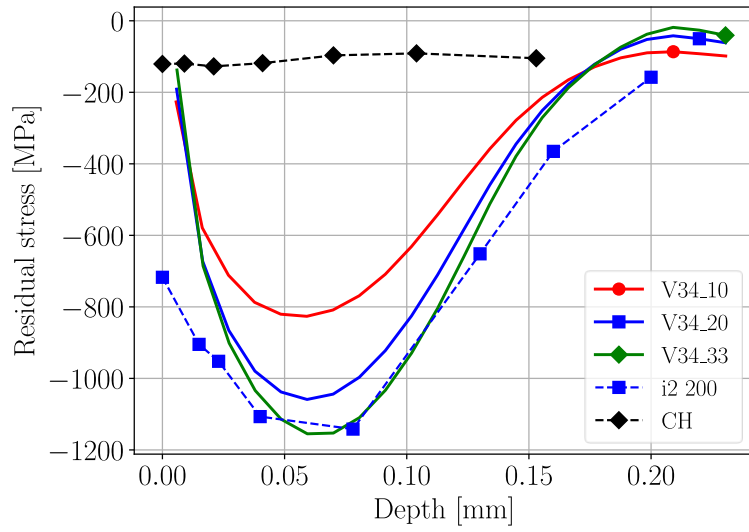


Figure 20: Residual stresses with simulated results at the 10th, 20th, and 33rd impact.

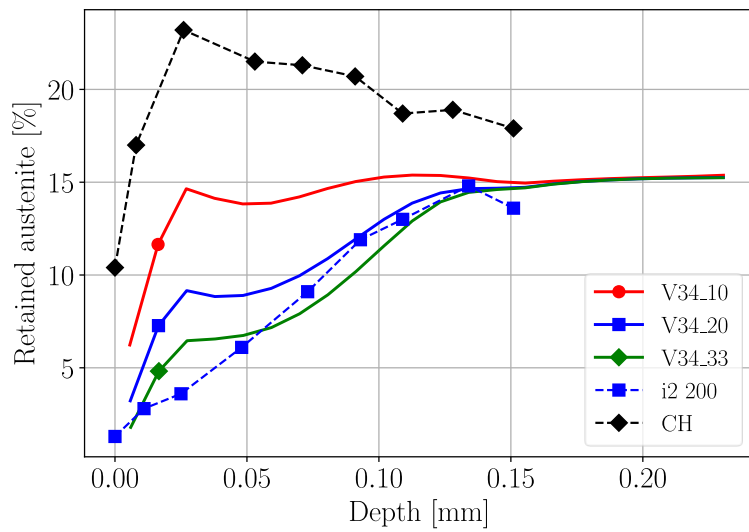


Figure 21: Retained austenite with simulated results at the 10th, 20th, and 33rd impact.

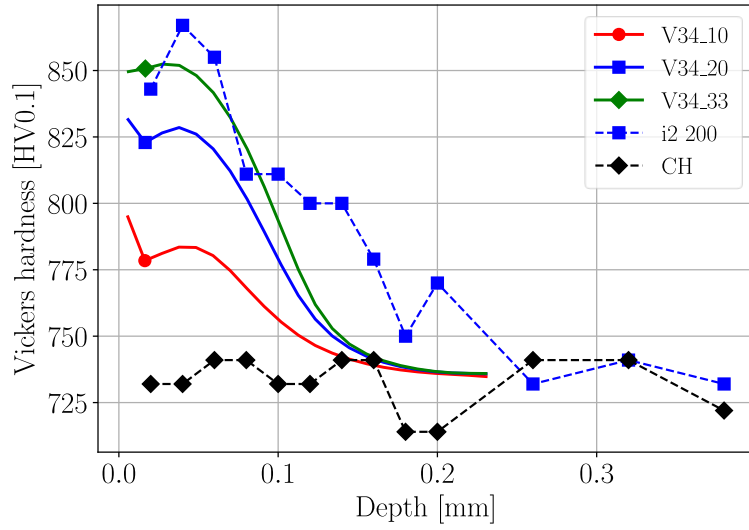


Figure 22: Vickers hardness with simulated results at the 10th, 20th, and 33rd impact.

5.8 Cross section results

The measured values for residual stress and retained austenite are an average of a circular measurement area of approximately 2 mm in diameter. The plotted simulated results are also computed as an average at each depth below the surface for the evaluation area of the target. The simulated results in a cross section of the target, Figure 23, indicate that the stresses are far from uniform. Some parts under the surface have substantially higher compressive stresses than nearby areas, depending on the positions and impact order of the media. The martensite content f_m , shown in Figure 24, is more evenly distributed than the residual stresses. This is probably due to the material model chosen, which does not include shear band induced transformation.

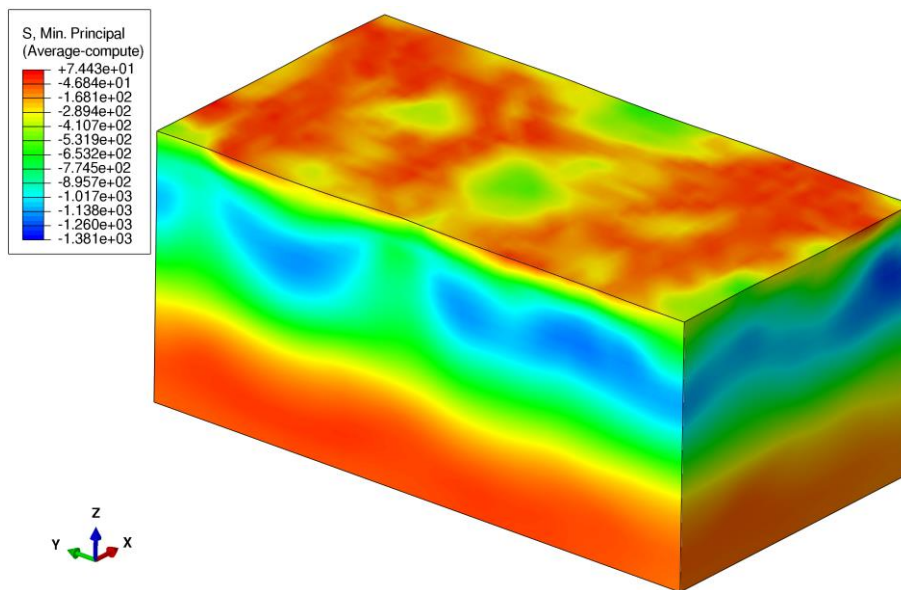


Figure 23: Residual stresses in a cross section through the middle of the evaluation area of the target.

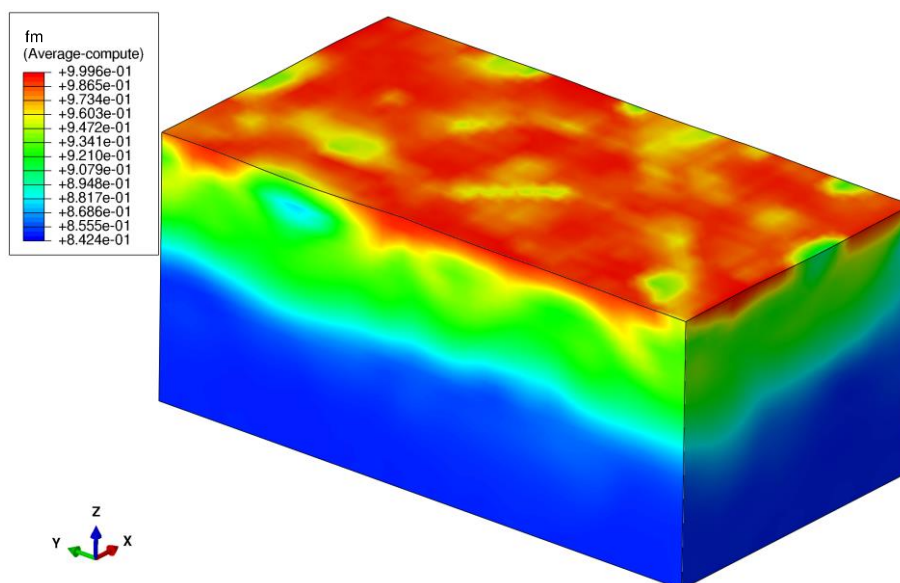


Figure 24: Martensite content in a cross section through the middle of the evaluation area of the target.

5.9 Media shape variation

As previously mentioned, normal shot peening balls are not perfectly spherical due to economic reasons. They are instead multifaceted shapes approximating spheres. At the moment of impacts there will therefore be a distribution of varying radii of curvature of the balls which interacts with the target. To give a simplified understanding of the impacts of this an ellipsoid shape is used instead of a true spherical. Depending on the choice of major and minor axis relations, impacting areas of the ball can be “pointed”, spherical or “flat” as shown in Figure 25. The dimensions of all three shapes are scaled so they have the same mass in all cases.

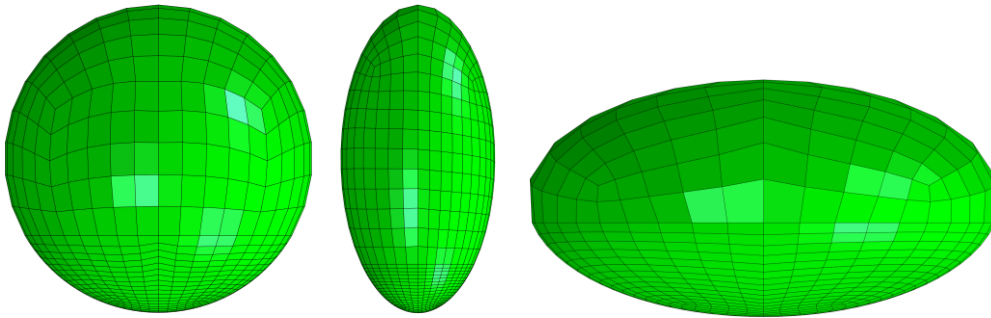


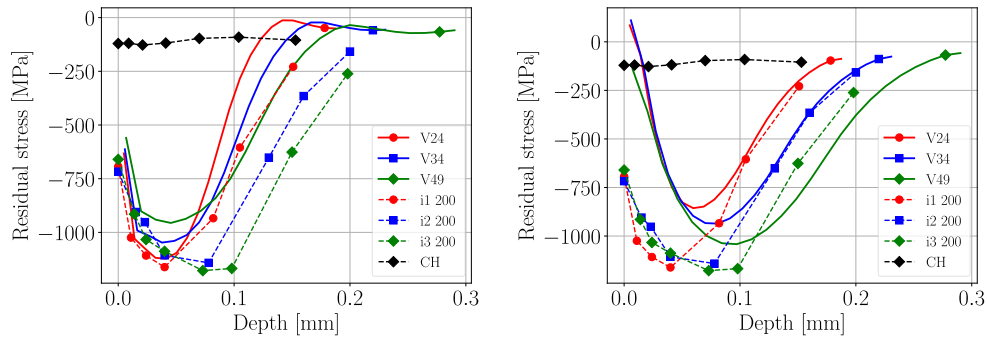
Figure 25: Mesh and shape for round, pointed and flat versions. Area that impacts target is down in all pictures. Sizes are not to scale. All balls have the same mass.

Figure 26 shows a comparison between pointed and flat impacts. The pointed impacts give more compressive residual stresses close to the surface, recreating quite well the experimental results. The flat impacts replicate the deeper stresses a little better than spherical shapes although the differences are smaller than for the surface stresses in the pointed case.

For the retained austenite results in Figure 27 the pointed impacts have a much closer grouping between the different intensities, similar

to the experimental results. The flat impacts have a large spread that does not correspond to the experimental results except very coarsely. It suggests that the flat impacts have less influence on retained austenite transformation experimentally than the simulation model gives.

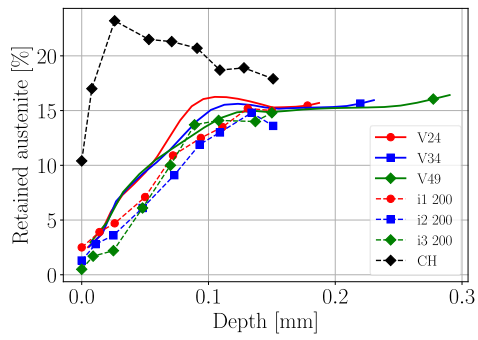
For the Vickers hardness values in Figure 28 the flat impacts seem to give better correlation to the measured values, giving increased hardness changes at deeper depths. The pointed impacts seem to only be important for the surface hardness increase.



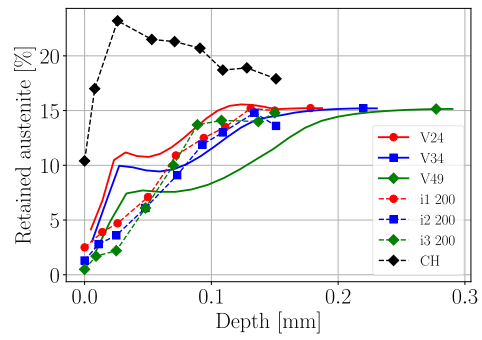
(a) Pointed impact shape

(b) Flat impact shape

Figure 26: Residual stress profiles with pointed impact shape (a) and flat impact shape (b)



(a) Pointed impact shape



(b) Flat impact shape

Figure 27: Retained austenite profile with pointed impact shape (a) and flat impact shape (b)

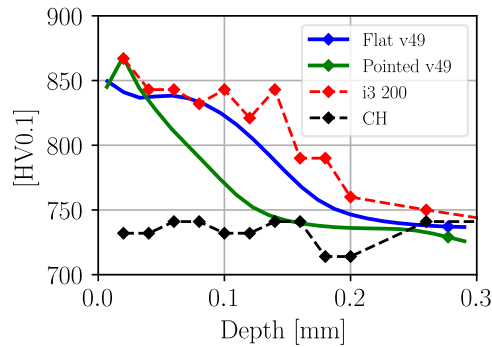
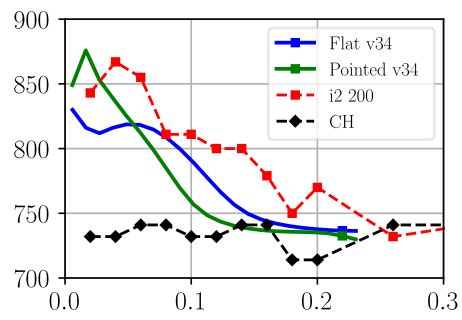
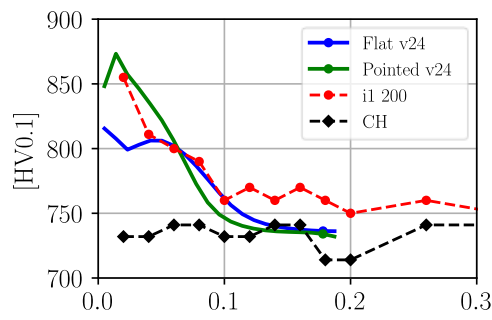


Figure 28: Vickers hardness with pointed or flat impact shape.

6 Discussion

The results from the media shape variations in Subsection 5.9 suggest that the experimental results are built up by a distribution of different ellipsoidal shapes. In addition, there is of course a distribution of masses of the media due to the sieve specifications. The velocity of the balls will also have a distribution when they impact the target and for shot peening of gear surfaces the angle of impact will also vary. In non-optimal situations, different parts of a target might also have different amount of coverage. Depending on how many passes over a certain area are chosen, this might have varying effect on the final results. So, there are several parameters, each with their own distributions, that together influence the final results on the target, just in the experimental case.

For the simulation, the chosen plasticity curve for the balls might be important. In this work, a realistic curve was chosen with the requirement that it passes through the stress point corresponding to the Vickers hardness at 8% plastic strain. No other information of the material behaviour of the media is known except the assumed elastic properties of steel and the Vickers hardness. Uniaxial testing of the initial wire material the media is made from, would not be useful because the media is severely deformed during the conditioning of the media. For the simulation, the chosen impact pattern will also influence. The Lombardo method does not account for the fact that two balls might interfere with each other, which will cause restrictions on how the impact pattern is created. Ricocheting balls will hit each other depending on the mass flow chosen for the shot peening. In severe cases media might be trapped and thereby shield certain parts of the target. A better impact pattern should therefore be simulated by DEM-methods [36, 37] and probably several variants should be simulated to understand how the results might vary at different positions on the target surface.

Modern tribological methods can now simulate the detailed interaction of two rough surfaces. Improved formulas for the oil film thickness also exist which should be used to design gear surfaces and compute the surface durability [38]. It should therefore be prioritized to continue work to create methods to effectively simulate shot peening on non-polished targets.

7 Conclusions

Overall it can be understood that simulating shot peening can become very complicated and computationally demanding. The model and simplification in this work does however result in trends that indicate what should be changed experimentally to reach a certain goal. With good accuracy, reasonable computer resources and basic experimental techniques to fit the model parameters, the model can predict:

- Residual stresses
- Retained austenite transformation
- Work hardening in form of Vickers hardness increase

The model is also adequate for parameter studies as exemplified by changing media hardness, coverage or media shape variations. Details in the residual stress, retained austenite and work hardening profiles seem to be predicted better by the media shape variations than spherical media with the material model chosen. Using only spherical media does however give good general results. For surface roughness predictions the initial surface roughness of the target must be included and future work is needed there.

Acknowledgement

The authors gratefully acknowledges the financial support from Scania CV AB.

References

1. Shot Peening APPLICATIONS NINTH EDITION METAL IMPROVEMENT COMPANY. (n.d.). Available at: https://www.cwst.co.uk/wp%2dcontent/uploads/2015/08/MIC_Green_Book_9th_Edition.pdf [Accessed 21 Sep. 2024].
2. Vrbka , M., Křupka , I., Svoboda P., Šperka P., Návrat T., Hartl, M. and Nohava J. (2011), Effect of shot peening on rolling contact fatigue and lubricant film thickness within mixed lubricated non-conformal rolling/sliding contacts, *Tribology International* 44:12, 1726-1735, DOI: 10.1016/j.triboint.2011.06.019
3. Li, W. and Liu, B. (2018), Experimental investigation on the effect of shot peening on contact fatigue strength for carburized and quenched gears, *International Journal of Fatigue* 106, 103-113, DOI: 10.1016/j.ijfatigue.2017.09.015
4. Hassani-Gangaraj, S.M., Cho, K.S., Voigt, H.-J.L., Guagliano, M. and Schuh, C.A. (2015), Experimental assessment and simulation of surface nanocrystallization by severe shot peening, *Acta Materialia* 97, 105-115, DOI: 10.1016/j.actamat.2015.06.054
5. Maleki, E., Unal, O. and Kashyzadeh, K.R. (2018), Effects of conventional, severe, over, and re-shot peening processes on the fatigue behavior of mild carbon steel, *Surface and Coatings Technology* 344, 62-74, DOI: 10.1016/j.surfcoat.2018.02.081

6. Nordin, E. and Alfredsson, B. (2017), Experimental investigation of shot peening on case hardened SS2506 gear steel, *Experimental Techniques* 41:4, 433-451, DOI: 10.1007/s40799-017-0183-4
7. Sidhoum, Z., Ferhoum, R., Almansba, M., Bensaada, R., Habak, M., Aberkane, M. (2018), Experimental and numerical study of the mechanical behavior and kinetics of the martensitic transformation in 304L TRIP steel: applied to folding, *International Journal of Advanced Manufacturing Technology* 97:5, 2757-2765, DOI: 10.1007/s00170-018-2154-z
8. Olson, G.B. and Cohen, M. (1975), Kinetics of strain-induced martensitic nucleation, 6:4, 791-795, DOI: 10.1007/BF02672301
9. Stringfellow, R.G., Parks, D.M., Olson, G.B. (1992), A constitutive model for transformation plasticity accompanying strain-induced martensitic transformations in metastable austenitic steels, *Acta Metallurgica Et Materialia* 40:7, 1703-1716, DOI: 10.1016/0956-7151(92)90114-T
10. Tomita, Y. and Iwamoto, T. (1995), Constitutive modeling of trip steel and its application to the improvement of mechanical properties, *International Journal of Mechanical Sciences* 37:12, 1295-1305, DOI: 10.1016/0020-7403(95)00039-Z
11. Serri, J., Martiny, M., Ferron, G. (2005), Finite element analysis of the effects of martensitic phase transformation in TRIP steel sheet forming, *International Journal of Mechanical Sciences* 47:6, 884-901, DOI: 10.1016/j.ijmecsci.2005.02.001
12. Sierra, R. and Nemes, J.A. (2008), Investigation of the mechanical behaviour of multi-phase TRIP steels using finite element methods, *International Journal of Mechanical Sciences* 50:4, 649-665, DOI: 10.1016/j.ijmecsci.2008.01.005

13. Guiheux, R., Berveiller, S., Kubler R., Bouscaud, D., Patoor, E., Puydt, Q. (2017), Martensitic transformation induced by single shot peening in a metastable austenitic stainless steel 301LN: Experiments and numerical simulation, *Journal of Materials Processing Technology* 249, 339-349, DOI: 10.1016/j.jmatprotec.2017.06.015
14. Neu, R.W. and Sehitoglu, H. (1992), Stress-induced transformation in a carburized steel-Experiments and analysis, *Acta Metallurgica Et Materialia* 40:9, 2257-2268, DOI: 10.1016/0956-7151(92)90144-4
15. Hazar, S., Alfredsson, B., Lai, J., (2018), Mechanical modeling of coupled plasticity and phase transformation effects in a martensitic high strength bearing steel, *Mechanics of Materials* 117, 41-57, DOI: 10.1016/j.mechmat.2017.10.001
16. Linares Arregui, I. and Alfredsson, B. (2010), Elastic–plastic characterization of a high strength bainitic roller bearing steel—experiments and modelling, *International Journal of Mechanical Sciences* 52:10, 1254 – 1268, DOI: 10.1016/j.ijmecsci.2010.06.001
17. Zimmermann, M., Klemenz, M., Schulze, V. (2010), Literature review on shot peening simulation, *International Journal of Computational Materials Science and Surface Engineering*, 3:4, 289-309, DOI: 10.1504/IJCMSSE.2010.036218
18. Meguid, S.A., Shagal, G., Stranart, J.C. and Daly, J. (1999), Three-dimensional dynamic finite element analysis of shot-peening induced residual stresses, *Finite Elements in Analysis and Design* 31:3, 179-191, DOI: 10.1016/S0168-874X(98)00057-2

19. Meguid, S.A., Shagal, G., Stranart, J.C. (2002), 3D FE analysis of peening of strain-rate sensitive materials using multiple impingement model, *International Journal of Impact Engineering*, 27:2, 119-134, DOI: 10.1016/S0734-743X(01)00043-4
20. Schwarzer, J., Schulze, V., Vöhringer, O. (2002), Finite element simulation of shot peening – A method to evaluate the influence of peening parameters on surface characteristics, In: L. Wagner (ed) *International Conferences on Shot Peening (ICSP-8)*, Munich, Germany
21. Miao, H.Y., Larose, S., Perron, C., Lévesque, M. (2009), On the potential applications of a 3D random finite element model for the simulation of shot peening, *Advances in Engineering Software* 40:10, 1023-1038, DOI: 10.1016/j.advengsoft.2009.03.013
22. Bagherifard, S., Ghelichi, R., Guagliano, M. (2012), Numerical and experimental analysis of surface roughness generated by shot peening, *Applied Surface Science* 258:18, 6831-6840, DOI: 10.1016/j.apsusc.2012.03.111
23. Wang, C., Hu, J., Gu, Z., Xu, Y., Wang, X. (2017), Simulation on Residual Stress of Shot Peening Based on a Symmetrical Cell Model, *Chinese Journal of Mechanical Engineering* 30:2, 344-351, DOI: 10.1007/s10033-017-0084-6
24. Nordin, E. and Alfredsson, B. (2016), Measuring shot peening media velocity by indent size comparison, *Journal of Materials Processing Technology* 235, 143-148, DOI: 10.1016/j.jmatprotec.2016.04.012
25. Chaboche, J.L., Dang Van, K., Cordier, G. Boley, B.A. (Ed.). (1979), *Modelization of the strain memory effect on the cyclic hardening of 316 stainless steel*. Netherlands: North-Holland Publishing Co.

26. Frederick, C.O. and Armstrong, P.J. (2007), A mathematical representation of the multiaxial Bauschinger effect, *Materials at High Temperatures*, 24:1, 1-26, DOI: 10.1179/096034007X207589
27. Koistinen, D.P. and Marburger, R.E. (1959), A general equation prescribing the extent of the austenite-martensite transformation in pure iron-carbon alloys and plain carbon steels, *Acta Metallurgica* 7:1, 59-60, DOI: 10.1016/0001-6160(59)90170-1
28. Denis, S., Gautier, E., Simon, A., Beck, G. (1984), Stress-phase-transformation interactions - basic principles, modelling, and calculation of internal stresses, 1:10, 805-814, DOI: 10.1179/mst.1985.1.10.805
29. Kubler, R., Berveiller, M. and Pascal Buessler (2011). Semi phenomenological modelling of the behavior of TRIP steels. *International journal of plasticity*, 27(3), pp.299–327. doi:<https://doi.org/10.1016/j.ijplas.2010.05.002>.
30. Mata, M., Alcalá, J. (2003), Mechanical property evaluation through sharp indentations in elastoplastic and fully plastic contact regimes, *Journal of Materials Research* 18:7, 1705-1709, DOI: 10.1557/JMR.2003.0234
31. Moyer, J.M.a and Ansell, G.S.b (1975), The volume expansion accompanying the martensite transformation in iron-carbon alloys, *Metallurgical Transactions A* 6:9, 1785-1791, DOI: 10.1007/BF02642308
32. JMatPro Sente Software. (2024). *JMatPro Sente Software - JMatPro®*. [online] Available at: <https://www.sentesoftware.co.uk/jmatpro/full-details> [Accessed 23 Sep. 2024].
33. Johnson, K.L. (1985), *Contact Mechanics*, Cambridge University Press, Cambridge, UK

34. Lombardo, D. and Bailey, P. (1996), The reality of shot peen coverage, In: J. Champaigne (ed) International Conferences on Shot Peening (ICSP-6), San Francisco, CA, USA
35. Tabor, D. (1951), The hardness of metals, Clarendon Press, Oxford
36. Tu, F., Delbergue, D., Miao, H., Klotz, T., Brochu, M., Bocher, P., Levesque, M. (2017), A sequential DEM-FEM coupling method for shot peening simulation, *Surface and Coatings Technology* 319, 200-212, DOI: 10.1016/j.surfcoat.2017.03.035
37. Nguyen, .V.B., Poh, H.J., Zhang, Y.W. (2014), Predicting shot peening coverage using multiphase computational fluid dynamics simulations, *Powder Technology* 256, 100-112, DOI: 10.1016/j.powtec.2014.01.097
38. Hansen, J., Björling, M., & Larsson, R. (2021). A new film parameter for rough surface EHL contacts with anisotropic and isotropic structures. *Tribology Letters*, 69(2), 37.